

Article

Nd_{2-x}Sr_xNiO₄ Solid Solutions: Synthesis, Structure and Enhanced Catalytic Properties of Their Reduction Products in the Dry Reforming of Methane

Oleg A. Shlyakhtin ^{1,*}, Grigoriy M. Timofeev ¹, Sergey A. Malyshev ^{1,2}, Alexey S. Loktev ^{3,4,5}, Galina N. Mazo ¹, Tatiana Shatalova ^{1,2,6}, Veronika Arkhipova ⁴, Ilya V. Roslyakov ^{5,6} and Alexey G. Dedov ^{3,4,5}

¹ Department of Chemistry, M.V. Lomonosov Moscow State University, 119991 Moscow, Russia

² Department of Materials Sciences, Shenzhen MSU-BIT University, Shenzhen 518172, China

³ A.V. Topchiev Institute of Petrochemical Synthesis, Russian Academy of Sciences, 119991 Moscow, Russia

⁴ Department of General and Applied Chemistry, Gubkin Russian State University of Oil and Gas, 119991 Moscow, Russia

⁵ N.S. Kurnakov Institute of General and Inorganic Chemistry, Russian Academy of Sciences, 119991 Moscow, Russia

⁶ Department of Materials Sciences, M.V. Lomonosov Moscow State University, 119991 Moscow, Russia

* Correspondence: oleg@inorg.chem.msu.ru

Abstract: Solid solutions Nd_{2-x}Sr_xNiO_{4±δ} (x = 0, 0.5, 1, 1.2, 1.4) with a K₂NiF₄ structure can be obtained from freeze-dried precursors. The end members of this series can be obtained at T ≥ 1000 °C only, while complex oxides with x = 1; 1.5 are formed at T ≥ 700 °C. Thermal analysis revealed the two stages of Nd_{2-x}Sr_xNiO_{4±δ} thermal reduction in a 10%H₂/Ar gas mixture that was completed at 900 °C. For x < 0.2, the reduction products demonstrated an exsolution-like morphology with Ni nanoparticles allocated at the surface of oxide grains. As-obtained nanocomposites with x = 0 and x > 1 revealed the outstanding catalytic activity and selectivity in the dry reforming of the methane (DRM) reaction at 800 °C with CH₄ conversion close to the thermodynamic values. The appearance of two different maxima of the catalytic properties of Ni/(Nd₂O₃,SrCO₃) nanocomposites could be affiliated with the domination of the positive contributions of Nd₂O₃ and SrCO₃, respectively.

Keywords: metal–oxide nanocomposites; multicomponent catalysts; complex oxide precursors; K₂NiF₄ structure; high temperature reduction; exsolution; dry reforming of methane



Citation: Shlyakhtin, O.A.; Timofeev, G.M.; Malyshev, S.A.; Loktev, A.S.; Mazo, G.N.; Shatalova, T.; Arkhipova, V.; Roslyakov, I.V.; Dedov, A.G. Nd_{2-x}Sr_xNiO₄ Solid Solutions: Synthesis, Structure and Enhanced Catalytic Properties of Their Reduction Products in the Dry Reforming of Methane. *Catalysts* **2023**, *13*, 966. <https://doi.org/10.3390/catal13060966>

Academic Editors: Georgios Bamos, Athanasia Petala and Zacharias Frontistis

Received: 6 May 2023

Revised: 29 May 2023

Accepted: 30 May 2023

Published: 2 June 2023

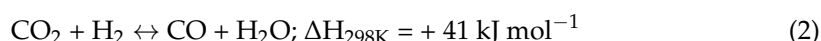
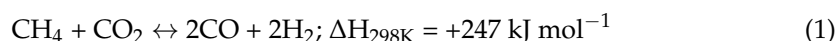


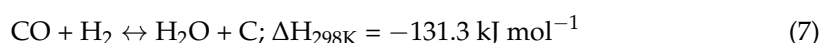
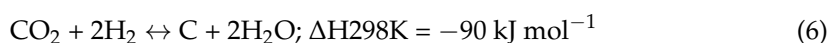
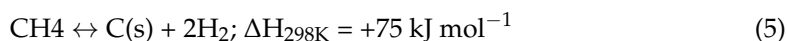
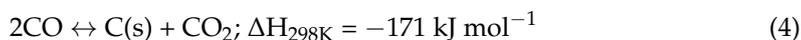
Copyright: © 2023 by the authors. Licensee MDPI, Basel, Switzerland. This article is an open access article distributed under the terms and conditions of the Creative Commons Attribution (CC BY) license (<https://creativecommons.org/licenses/by/4.0/>).

1. Introduction

Through the dry reforming of methane (DRM), the reaction of methane with CO₂ is one of the most prospective methods of methane conversion into synthesis gas and is a useful raw material for the large-scale chemical industry. The advantage of DRM in the steam reforming of methane currently available on large-scale deals with a more balanced composition of Syngas is that it allows its direct processing into petrochemical products. Another advantage of DRM is that it deals with the utilization of significant amounts of CO₂ byproducts which are often formed in other petrochemical and other industrial processes. In addition, more and more attention is being paid to the dry reforming of methane to a synthesis gas as an effective way to utilize these two main greenhouse gases [1–5]. The DRM process is also rather beneficial for utilization and conversion into value-added products with the growing amounts of biogas consisting mostly of CH₄ and CO₂ [6,7].

The main processes that occurred during DRM is shown as follows [1,2,8–10]:





The main reaction (1) of the DRM process was strongly endothermic due to the large amount of energy necessary to break down methane and CO_2 . According to thermodynamic calculations, the equilibrium was shifted to CO and H_2 at $T > 640$ °C. The amount of these reaction products increased with the temperature and in the lack of catalyst approaches 100% at $T = 1000$ – 1100 °C. The actual composition of the reaction mixture depended on the reaction rate and the contribution of the side reactions (2)–(5). The amount of hydrogen in the reaction products could be reduced by a reverse water-gas shift reaction (2). The reaction of methane and CO_2 could also cause the formation of hydrocarbons through a reaction (3) through one of the main obstacles to the large-scale application of DRM were reactions (4) and (5) and, to a lesser extent, (6) and (7), which caused the formation of coke at the surface of the catalysts and resulted in their deterioration [11].

Due to these features, DRM is usually performed as a catalytic process; the possibility of realizing it with a high yield of products at reasonable temperatures depends greatly on the selection of efficient catalysts. This selection deals with features of the DRM reaction mechanism at the atomic level. According to the existing models, the DRM reaction in the catalytic mode could be divided into four elementary steps: (1) the dissociative adsorption of methane at the metal surface and fast desorption of H_2 ; (2) the dissociative adsorption of CO_2 at the metal and metal–oxide interface and fast desorption of CO ; (3) formation of the surface hydroxyl groups by hydrogen and oxygen spillover at the surface of the catalyst; (4) the oxidation of methyl-like CH_x groups by the surface oxygen and hydroxyls, resulting in the formation and desorption of CO and H_2 [10,12,13].

The highest activity and selectivity in DRM among the base metals was demonstrated by the nickel catalysts, especially at $T < 900$ °C. The main problem with their industrial application is related to intense coking which results in the progressive deactivation of the catalyst. However, recent studies of the coking processes demonstrated that their intensity could be significantly reduced by the particle size control and selection of oxide substrates. Taking into account the atomic scale model of the DRM process, the oxide substrate is now considered one of the key elements of metal–oxide composite catalysts, as the sorption and activation of CO_2 usually occur at the oxide components of catalysts. It was found that the surface acidity/basicity of the oxide components was rather important for this process, which made it preferable to the application of alkaline earth and rare earth oxides, such as the elements of DRM catalysts [8]. Several other, more complex metal–oxide interactions could also be important in DRM catalysis. It was found, for example, that the methane activation barriers were drastically different for Co and Ni surfaces of pure metals and for $\text{Co}/\text{CeO}_{2-x}$ (111) and $\text{Ni}/\text{CeO}_{2-x}$ (111) surfaces [10,14,15]. These features make the processes of metal–oxide interaction in the catalytic systems one of the hottest topics in modern studies of heterogeneous catalysts.

Until now, most of the metal-oxide catalysts have been prepared by the incipient wetness technique when the porous oxide substrate is soaked with a solution containing active metal, followed by drying, thermal decomposition, and the chemical reduction in the metal-containing component. This method ensures the relatively uniform distribution of catalytically active components across the surface of the supporting material. Along

with the preferences for their chemical composition described before, these materials should possess a high surface area, extended porosity, and excellent thermal stability. A significant interaction of the active metal with the oxide surface is considered a positive factor here, as the anchoring of active particles to the surface of the supporting material promotes the prevention of sintering the nanoparticles of active metals in the reaction environment which is the second most important reason for catalyst deactivation. However, this method is really efficient when the composite metal-oxide catalyst consists of a single active component and a single supporting material only [11].

Due to the multistage mechanism of the DRM process, the modern Ni-based DRM catalysts usually consist of several components promoting the most efficient realization of the particular stages of the process [10]. To implement the efficient transport of the adsorbed reaction species between these components, it is necessary to provide a number of tight multiphase contacts of the various catalyst components. One of the best ways to ensure that multiphase contacts are based on a reduction in the complex oxide precursors containing all the necessary cations. The application of single oxide precursors ensures the reproducibility not only of the phase composition but also the morphology of the catalyst [1].

Currently, the most often used precursors are complex oxides with *q* perovskite structure, though, in the case of nickel-based catalysts, the number of suitable perovskites is rather limited. The largest number of studies in this field deal with LaNiO_3 and its solid solutions. The preliminary chemical reduction in this complex oxide, often called the activation of the catalyst, results in the formation of a Ni/ La_2O_3 nanocomposite when the nanoparticles of the Ni metal are allocated at the surface of lanthanum oxide. The processing of native LaNiO_3 at DRM conditions also results in the fast decomposition of LaNiO_3 , which usually occurs through the formation of the $\text{La}_2\text{O}_2\text{CO}_3$ intermediate. Despite the same phase composition of reduction products in both cases, different reaction routes cause a different Ni particle size and a different character of its spatial distribution. Taking into account the reversibility of $\text{La}_2\text{O}_2\text{CO}_3$ decomposition and the closeness of its decomposition temperature and usual processing conditions of the DRM process ($T = 700\text{--}800\text{ }^\circ\text{C}$; CO_2 -containing atmosphere), the actual composition of the nanocomposite catalyst, in this case, is rather Ni/ $\text{La}_2\text{O}_2\text{CO}_3$ than Ni/ La_2O_3 . The temperature of the reductive decomposition of LaNiO_3 and, hence, the morphology of its decomposition products could be substantially modified by the cationic substitution both to La- and to Ni-sublattices of the perovskite structure by Ca, Sr, Ce, and by Fe, Mn, respectively. The easy resynthesis of LaNiO_3 from the spent catalyst at moderate temperatures in the air promotes its oxidative regeneration, followed by its further reduction to Ni/(La_2O_3 , $\text{La}_2\text{O}_2\text{CO}_3$) nanocomposites [16,17].

The number of the available Ni-containing complex oxides with the K_2NiF_4 structure is much larger, which opens a broader selection of the possible metal-oxide compositions that can be obtained by their thermal reduction [18]. Our previous studies demonstrated the efficiency of the metal-oxide nanocomposites obtained by the thermal reduction of $(\text{Ln,Ca})_2(\text{Ni,Co})\text{O}_4$ as catalysts for the partial oxidation and dry reforming of methane [19–21]. The essential morphological feature of as-obtained composites is the formation of the Ni metal nanoparticles at the surface of larger agglomerates of the oxide-based reduction products. This type of composite is usually observed before in the course of several processes of a partial reduction in complex oxides (redox exsolution) and is characterized by the enhanced strength of the metal particle connection with a surface of oxide particle [22–24]. The DRM catalysts based on these composites and obtained by both a partial or complete reduction in oxides were found prone not only to the sintering of active metal particles in the course of the DRM process but also to intense coking at their surface: one of the main reasons for the deactivation of DRM catalysts [25,26].

The best catalysts of the DRM at $T < 800\text{ }^\circ\text{C}$ among these products were the Ni/(Nd_2O_3 , CaO) nanocomposites obtained by the thermal reduction of $(\text{Nd,Ca})_2\text{NiO}_4$ [20]. To find the most efficient one among them, it was necessary to vary their composition and compare their properties. However, the homogeneity range of these solid solutions was found to

be rather limited ($0 < x < 0.5$), which, in turn, limited the variation range of these metal–oxide composites by the Nd/Ca ratio. It is known that the variation range was wider for $\text{Nd}_{2-x}\text{Sr}_x\text{NiO}_4$ solid solutions [27], and their reduction products were also expected to be good DRM catalysts. Similarly to LaNiO_3 -derived catalysts, SrO in the Ni/(Nd_2O_3 , SrO) composite could transform into SrCO_3 in the DRM environment. Apart from $\text{La}_2\text{O}_2\text{CO}_3$, the information on the SrCO_3 effect on the properties of DRM catalysts was rather limited. However, the high thermal stability of SrCO_3 , especially in a CO_2 -containing DRM environment, could promote the morphological stabilization of the composite Ni/(Nd_2O_3 , SrCO_3) catalyst at elevated temperatures.

Due to these reasons, the present study was aimed at the synthesis of $\text{Nd}_{2-x}\text{Sr}_x\text{NiO}_4$ complex oxides, the refinement of the homogeneity ranges of these solid solutions with K_2NiF_4 structure in the air, the study of their thermal reduction processes, an analysis of the composition and morphology of their reduction products and evaluation of their catalytic properties in the DRM reaction.

2. Results and Discussion

In order to investigate the thermal decomposition features of the freeze-dried precursors, TG measurements with a simultaneous DSC signal detection were carried out for two samples of significantly different compositions. It was observed that both Nd_2NiO_4 and $\text{Nd}_{0.6}\text{Sr}_{1.4}\text{NiO}_4$ precursors exhibited rather similar behavior in the course of their TG-DSC examination (Figures S1 and S2). Their TG profiles contained three distinct temperature ranges that likely corresponded to the different chemical reactions that occurred in precursors. The first step at ~ 150 – 250 °C could be attributed to the elimination of chemically bound water presented as $-\text{OH}$ species or H_2O molecules incorporated into the structure of inorganic hydrates. The second step at 250 – 400 °C corresponded to the decomposition of Nd, Sr, and Ni nitrates, and the last step was likely to be the complete combustion of PVA fragments by atmospheric O_2 or/and active oxygen species released during the decomposition of nitrates at temperatures near the combustion reaction. The combustion nature of this process was confirmed by a strong exothermic effect at 400 – 450 °C, which was detected by the DSC method. No effects at temperatures above 500 °C were observed in the TG-DSC profiles except a slight mass loss at 850 – 900 °C for the $\text{Nd}_{0.6}\text{Sr}_{1.4}\text{NiO}_4$ precursor. This could have been elucidated by the decomposition of the minor amount of SrCO_3 formed by the partial interaction of SrO with CO_2 gas released in the course of PVA combustion. Thus, the intensive formation of the target K_2NiF_4 complex oxides under isothermal temperature conditions was expected at $T > 500$ – 600 °C after the completion of all decomposition/combustion processes in freeze-dried precursors.

To study the complex oxide formation, the thermal decomposition of the freeze-dried precursors was performed in the air at $T = 600$ – 1200 °C for 6 h. A careful comparison of the XRD patterns of the decomposition products revealed the considerable dependence of the phase formation conditions on the $\text{Nd}_{2-x}\text{Sr}_x\text{NiO}_4$ composition (Figure 1 and Figures S3–S7).

In the case of Nd_2NiO_4 , the samples obtained at 600 – 700 °C consisted of a mixture of cubic Nd_2O_3 and NdNiO_3 with an orthorhombic perovskite structure. These observations were in good accordance with the fact that neodymium-nickel perovskite can be obtained at lower temperatures under an air atmosphere [28]. Further heating provided a solid-state interaction between Nd_2O_3 and NdNiO_3 , forming the target Nd_2NiO_4 compound at $T > 900$ °C.

In the case of $\text{Nd}_{1.5}\text{Sr}_{0.5}\text{NiO}_4$ and NdSrNiO_4 compositions, the thermal decomposition of the freeze-dried precursors led to the intense dominant formation of the target K_2NiF_4 phases even at 600 – 700 °C; only trace amounts of the SrCO_3 carbonate was observed by XRD. All the samples obtained at $T \geq 800$ °C were single-phase complex nickelates. Such low temperatures demanded $\text{Nd}_{1.5}\text{Sr}_{0.5}\text{NiO}_4$ and NdSrNiO_4 formation to be explained by the drastic stabilization of the K_2NiF_4 structure due to the substitution of Nd^{3+} with a larger Sr^{2+} cation.

	Nd_2NiO_4	$\text{Nd}_{1.5}\text{Sr}_{0.5}\text{NiO}_4$	NdSrNiO_4	$\text{Nd}_{0.8}\text{Sr}_{1.2}\text{NiO}_4$	$\text{Nd}_{0.6}\text{Sr}_{1.4}\text{NiO}_4$
1100 °C	Nd_2NiO_4	$\text{Nd}_{1.5}\text{Sr}_{0.5}\text{NiO}_4$	NdSrNiO_4	$\text{Nd}_{0.8}\text{Sr}_{1.2}\text{NiO}_4$	$\text{Nd}_{0.6}\text{Sr}_{1.4}\text{NiO}_4$
1000 °C	Nd_2NiO_4	$\text{Nd}_{1.5}\text{Sr}_{0.5}\text{NiO}_4$	NdSrNiO_4	$\text{Nd}_{0.8}\text{Sr}_{1.2}\text{NiO}_4$	$\text{Nd}_{0.6}\text{Sr}_{1.4}\text{NiO}_4$
900 °C	Nd_2NiO_4	$\text{Nd}_{1.5}\text{Sr}_{0.5}\text{NiO}_4$	NdSrNiO_4	$\text{Nd}_{0.8}\text{Sr}_{1.2}\text{NiO}_4$	RP P
800 °C	RP c- Nd_2O_3 P	$\text{Nd}_{1.5}\text{Sr}_{0.5}\text{NiO}_4$	NdSrNiO_4	RP SrCO_3	RP P
700 °C	P c- Nd_2O_3	$\text{Nd}_{1.5}\text{Sr}_{0.5}\text{NiO}_4$	RP SrCO_3	RP SrCO_3	RP SrCO_3
600 °C	P c- Nd_2O_3	RP SrCO_3	RP SrCO_3	RP SrCO_3	RP SrCO_3

Figure 1. The phase composition of $\text{Nd}_{2-x}\text{Sr}_x\text{NiO}_4$ samples obtained at various temperatures; RP—oxide with K_2NiF_4 structure, P—oxide with perovskite structure.

According to the XRD data, the thermolysis products at 600–700 °C contained phases with a K_2NiF_4 structure mixed with considerable amounts of strontium carbonate. Apparently, these K_2NiF_4 products were stable complex nickelates with a moderate Sr content; the excess of the last one was presented as a SrCO_3 phase. Interestingly, further heating to 800–900 °C led to the formation of mixtures of K_2NiF_4 and orthorhombic perovskite phases. A similar feature was observed for Nd-Ca cobaltite in [29], where the formation of the target K_2NiF_4 complex oxide at moderate temperatures was accompanied by the kinetically controlled formation of an intermediate phase with a perovskite structure. For Nd-Sr nickelates, the observed features could be explained by the formation of Sr-rich (Nd,Sr) NiO_3 perovskites with a Ni oxidation state close to +3 followed by their solid state interaction with the “low temperature” Nd-rich (Nd,Sr) $_2\text{NiO}_4$ phases at 900–1000 °C, resulting in the target $\text{Nd}_{0.8}\text{Sr}_{0.2}\text{NiO}_4$ and $\text{Nd}_{0.6}\text{Sr}_{1.4}\text{NiO}_4$ nickelates.

Thus, despite such diverse solid-state reaction pathways, all the discussed nickelates could be securely synthesized by the freeze-drying method at $T = 1000\text{--}1200$ °C in the air. In order to ensure a high level of crystallographic ordering in such multicomponent solid solutions and to make a reliable comparison between the samples with various Sr content, a series of $\text{Nd}_{2-x}\text{Sr}_x\text{NiO}_4$ samples ($x = 0; 0.5; 1; 1.2; 1.4$) obtained at 1200 °C was chosen for further investigation. According to the XRD study, their crystal structure was reliably assigned to the perovskite-related K_2NiF_4 type. Similarly to [20], the orthorhombically distorted Fmmm structure was observed for Nd_2NiO_4 ($x = 0$); no additional reflections of the other K_2NiF_4 polymorphs were observed. On the other hand, for the Sr-containing solid solutions ($0.5 \leq x \leq 1.4$), a tetragonal I4/mmm structure was verified (Figure 2). It clearly indicated the stabilization effect. A profile analysis of these complex oxides was performed by the Le Bail method from powder XRD data; the resulting unit cell parameters are given in Table 1.

The variation in the K_2NiF_4 lattice parameters values on the Sr content was found similar to that found in [27]. It is noteworthy that the observed changes could be attributed to both Nd/Sr and O stoichiometry which provided a notable deviation from the linear Vegard’s rule (Figure S8). The absence of these changes for the sample with $x > 1.4$ corresponded quite well with the previous conclusion on the allocation of the limit of the $\text{Nd}_{2-x}\text{Sr}_x\text{NiO}_{4\pm\delta}$ homogeneity range at $1.4 < x < 1.6$.

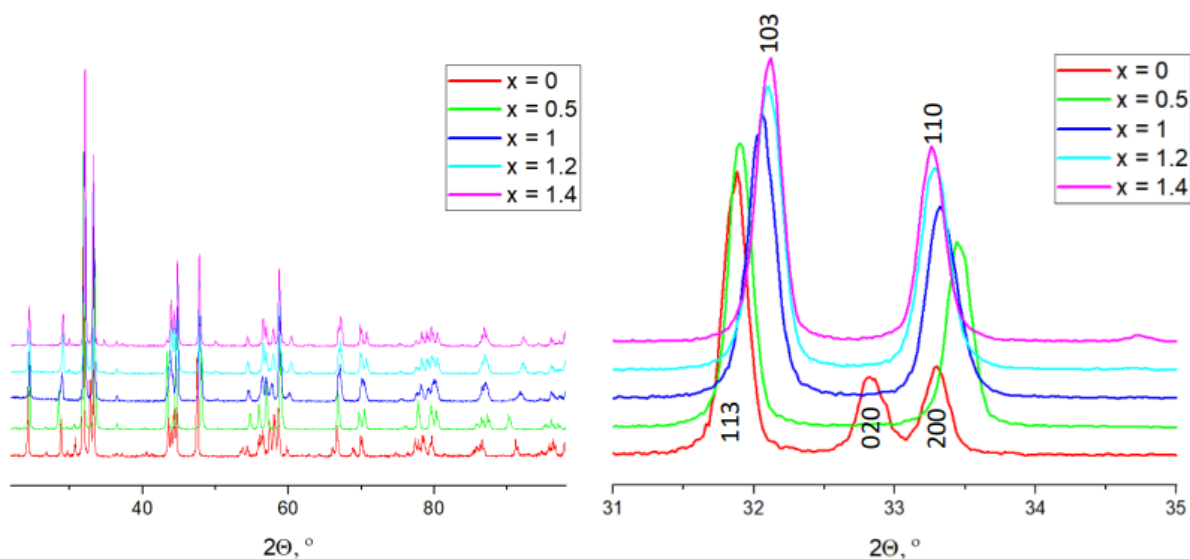


Figure 2. XRD patterns of $\text{Nd}_{2-x}\text{Sr}_x\text{NiO}_4$ obtained at $T = 1200^\circ\text{C}$.

Table 1. The unit cell parameters of $\text{Nd}_{2-x}\text{Sr}_x\text{NiO}_{4\pm\delta}$.

Composition	Space Group	a, Å	b, Å	c, Å	V, Å ³
$\text{Nd}_2\text{NiO}_{4\pm\delta}$	Fmmm	5.3789(3)	5.4514(3)	12.3724(8)	362.79(5)
$\text{Nd}_{1.5}\text{Sr}_{0.5}\text{NiO}_{4\pm\delta}$	I4/mmm	3.776(2)	3.776(2)	12.482(1)	177.9(2)
$\text{NdSrNiO}_{4\pm\delta}$	I4/mmm	3.7886(2)	3.7886(2)	12.320(1)	176.8(2)
$\text{Nd}_{0.8}\text{Sr}_{1.2}\text{NiO}_{4\pm\delta}$	I4/mmm	3.798(2)	3.798(2)	12.261(1)	176.8(2)
$\text{Nd}_{0.6}\text{Sr}_{1.4}\text{NiO}_{4\pm\delta}$	I4/mmm	3.804(2)	3.804(2)	12.252(6)	177.3(2)
$\text{Nd}_{0.4}\text{Sr}_{1.6}\text{NiO}_{4\pm\delta}$	I4/mmm	3.8027(3)	3.8027(3)	12.266(11)	177.38(3)

The thermal analysis of the reduction processes of the as-obtained complex oxides in the Ar/H₂ mixture revealed two different stages of this process for all samples in the study (Figure 3A–C), as it was observed before for other K₂NiF₄ complex oxides [19–21]. According to the XRD analysis results of the reduction products, the partial reduction in the complex oxide precursor at the first stage caused its transformation into another complex oxide with an individual crystal structure. The detection of the Ni⁰ phase possibly formed during its reduction was complicated by the strong overlapping of its reflections with the reflections of complex oxide structures. Complete decomposition of this intermediate at the second stage of the reduction resulted in the formation of Ni⁰, Nd₂O₃, and SrO, which could be transformed into Sr(OH)₂ during further cooling in the air (Figure 3D). An increase in the Sr content in the initial complex oxide was accompanied by a systematic increase in the complete reduction temperature.

The microstructure of the complete reduction products of $\text{Nd}_{2-x}\text{Sr}_x\text{NiO}_{4\pm\delta}$ was similar to the microstructure in the reduction products of their Ca-substituted counterparts, as studied in more detail before. According to [19,20], the coarser grains were likely formed by Nd and Sr oxides that were coated with spherical nanoparticles of the Ni metal. Due to a wider range of Sr substitution in Nd_2NiO_4 compared to Ca, it was possible to observe in this case that the increase in Sr content was accompanied by a significant coarsening of the exsolved Ni particles from ~20 nm for $x = 0$ to 40–60 nm for $x \geq 1$, probably due to a higher reduction temperature (Figure 4C,D).

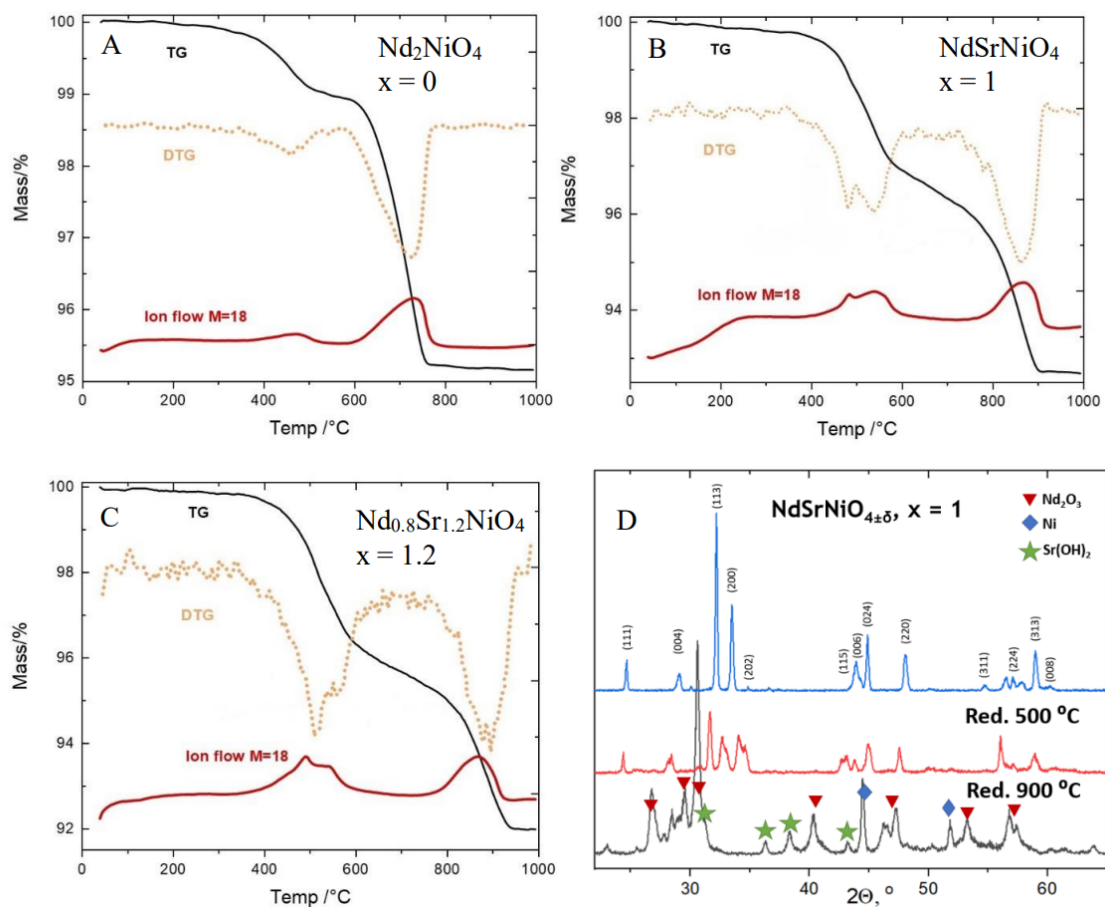


Figure 3. TG, DTG, and H_2O evolution curves for the reduction of Nd_2NiO_4 (A), NdSrNiO_4 (B), $\text{Nd}_{0.8}\text{Sr}_{1.2}\text{NiO}_4$ (C) in Ar/ H_2 mixture; XRD patterns of NdSrNiO_4 and its reduction products at 500 °C and 900 °C (D).

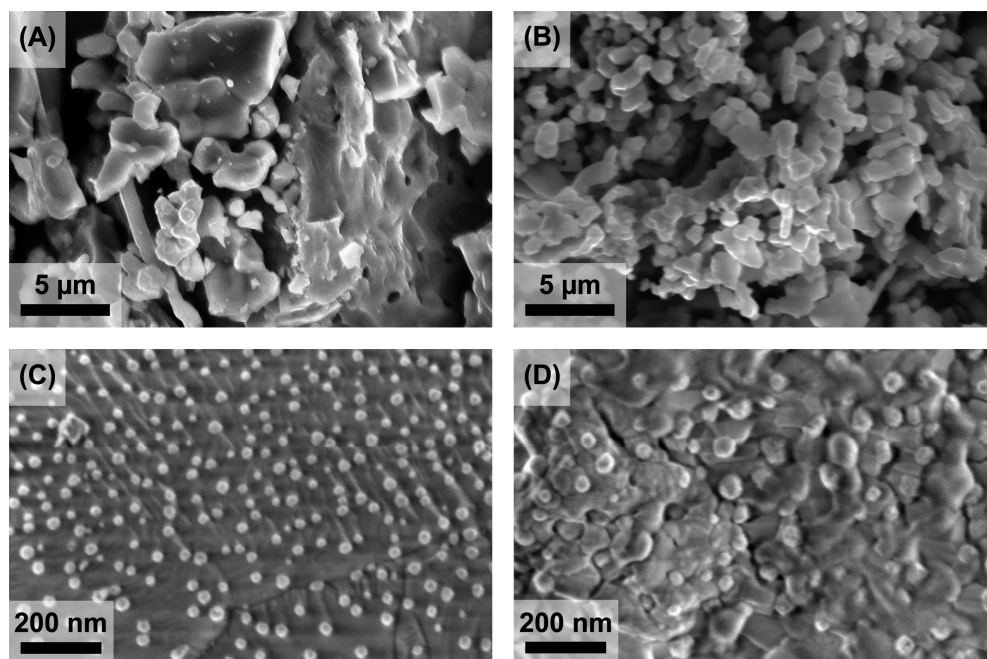


Figure 4. SEM micrographs of Nd_2NiO_4 (A), NdSrNiO_4 (B), and the products of their thermal reduction at 900 °C ((C,D), respectively).

Taking into account the results of our previous studies, it was expected that the reduction products of $\text{Nd}_{2-x}\text{Sr}_x\text{NiO}_{4\pm\delta}$ with the morphology described before would demonstrate significant catalytic properties in the DRM process. Due to the similarity of the catalytic processes, the DRM catalysts often demonstrated significant catalytic activity and selectivity in the partial oxidation of the methane (POM) reaction: another widely discussed alternative to the currently applied steam reforming process [2,19–21]. However, the production of syngas by DRM at $T = 700\text{--}800\text{ }^\circ\text{C}$ over the Ni-based catalysts could be more efficient than POM. According to [20], a lower CO yielded in POM at $T < 800\text{ }^\circ\text{C}$ over Ni/(Nd_2O_3 ,CaO) nanocomposites dealt with Ni oxidation to NiO, the catalyst of the total oxidation of methane and CO to CO_2 . The oxidation of the part of methane to CO_2 led to a notable decrease in syngas selectivity. Similar processes were expected to be obtained in $\text{Nd}_{2-x}\text{Sr}_x\text{NiO}_{4\pm\delta}$ -derived nanocomposites in the POM environment, but their appearance during DRM was less probable due to the lack of oxidants.

An experimental evaluation of their catalytic performance confirmed a considerable catalytic activity and selectivity in DRM for all metal–oxide composites in a study at $T \geq 700\text{ }^\circ\text{C}$ (Figure 5, Figures S9 and S10). However, the catalytic behavior of these composites demonstrated several important anomalies. Similar metal–oxide composites obtained from K_2NiF_4 -like precursors usually demonstrate a monotonous dependence of their catalytic properties in DRM both on the temperature and on the rare earth to alkaline earth ratio in the composite [19,20]. In the present case, the samples in the study could be divided into two different groups according to the behavior of their catalytic properties—Sr-free and Sr-containing composites. The catalytic activity and selectivity of the only member of the first group, the Nd_2NiO_4 reduction product ($x = 0$), similarly to [19,20], increased monotonously with the temperature demonstrating maximum values at the maximum temperature of the study ($T = 900\text{ }^\circ\text{C}$) and approaching their thermodynamic limits (Figure 5A and Figure S9B). Meanwhile, the maximum values of activity and selectivity in all the Sr-containing composites ($0.5 \leq x \leq 1.4$) were observed at $T = 800\text{ }^\circ\text{C}$ while further heating to $T = 900\text{ }^\circ\text{C}$, contrary to the thermodynamically predicted behavior, caused a considerable decrease in their catalytic performance. Another unusual feature in this series of composites dealt with a significant drop in catalytic activity at $0 < x \leq 0.5$. However, the further substitution of Nd with Sr resulted in the systematic recovery of the catalytic activity and selectivity of composites with their maximal values at $T = 800\text{ }^\circ\text{C}$ for the samples with $x = 1.2\text{--}1.4$.

The XRD analysis of spent catalysts revealed that they consisted of Ni and Nd_2O_3 for $x = 0$ and Ni, Nd_2O_3 , and SrCO_3 in all other cases (Figure 6A), as SrO converted easily into SrCO_3 in the DRM reaction environment [30]. Hence, the most probable reasons for the different behaviors of these two types of DRM catalysts were likely affiliated with the appearance of SrCO_3 in the composite catalysts and with specific properties of strontium carbonate. According to the existing models of DRM catalysis, the catalytic properties of the Nd_2NiO_4 reduction products were determined by the combination of the methane sorption and catalytic activity of nickel metal and the CO_2 sorption activity of the neodymium oxide. As the amount of Ni metal was almost the same in all samples in the study, the higher catalytic activity of the composites with a larger Sr content could be affiliated with more intense CO_2 sorption due to a higher basicity catalyst surface. However, a decrease in the sorption activity at higher temperatures was likely more pronounced for SrCO_3 than for Nd_2O_3 , thus promoting a definite decrease in the other catalytic properties of Sr-containing composites at $T > 800\text{ }^\circ\text{C}$.

The reasons for the observed drop in the catalytic properties at $0 < x \leq 0.5$ and, in general, the non-monotonous dependence of the catalytic properties of Ni/($\text{Nd}_{2-x}\text{Sr}_x$)O_y composites on x were likely due to a competition between the two catalytic pathways, via Nd_2O_3 and via SrCO_3 . It should also be noted that the catalytic activity of samples ($x = 1.2; 1.4$) with a larger size of Ni particles was the same or even higher than the corresponding activity of the Sr-free ($x = 0$) sample with much smaller Ni exclusions (Figure 4C,D). It appeared contradictory to the common trend of the better catalytic perfor-

mance of the smaller particles of a catalyst. This discrepancy could also be affiliated with different mechanisms of the DRM catalysis on Nd_2O_3 and SrCO_3 substrates when more efficient CO_2 activation with SrCO_3 became more important than the smaller activity of coarser Ni particles on the SrCO_3 substrate.

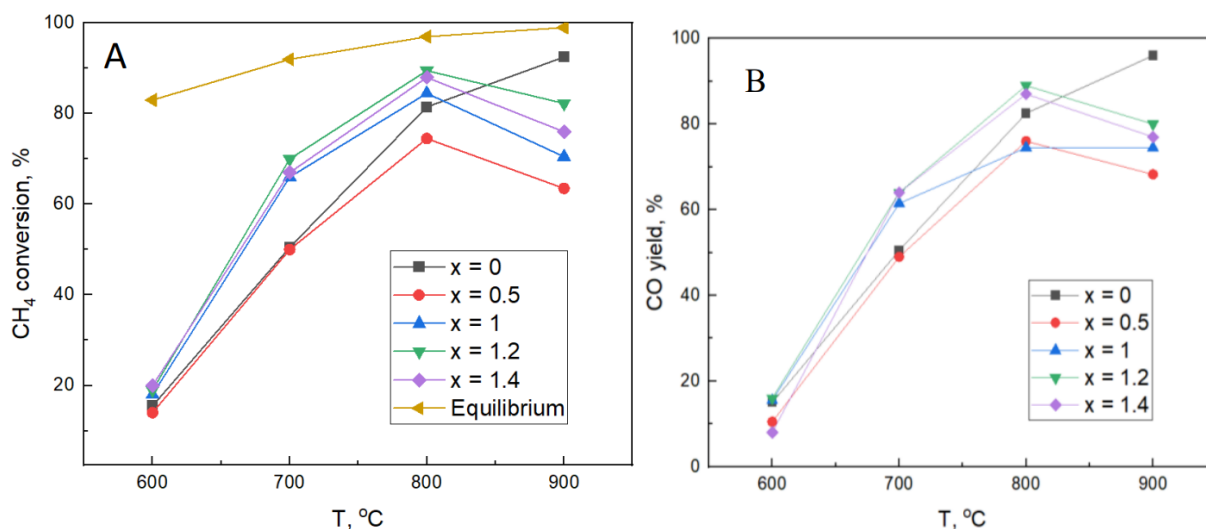


Figure 5. CH_4 conversion (A) and CO yield (B) over the reduction products of various composites. The calculated values of CH_4 conversion are given according to [13,31–33].

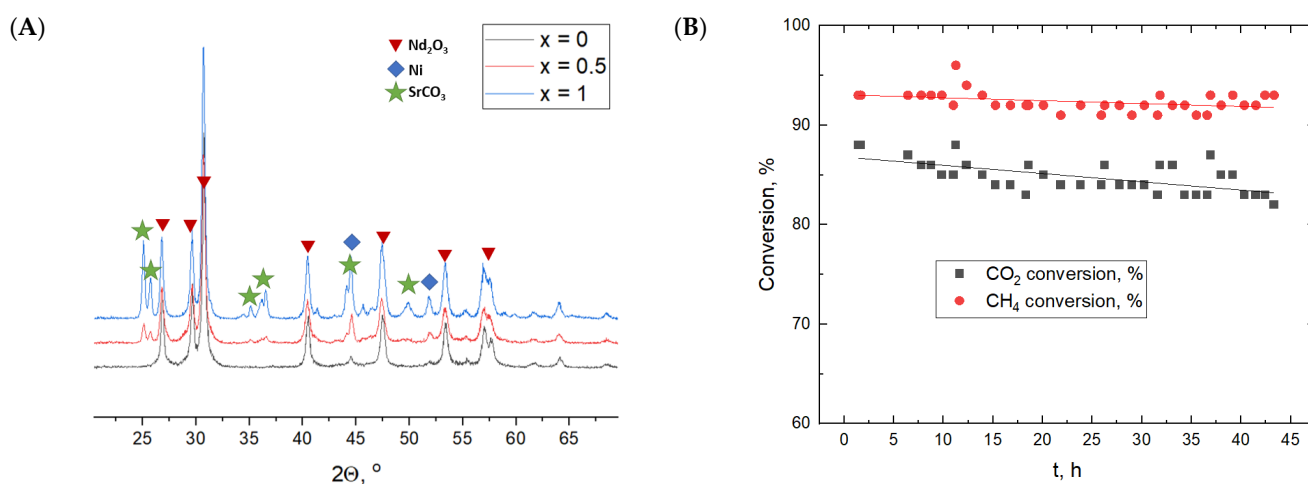


Figure 6. XRD patterns of spent catalysts (A) and the results of the stability test of the metal–oxide nanocomposite with $x = 1.4$ at $T = 800\text{ }^\circ\text{C}$ (B).

These interesting and unusual features demanded more detailed studies using modern instrumental methods. It should be noted, however, that the values of the activity and selectivity of as-obtained DRM catalysts were comparable with the results obtained by other groups [3,4,10,30,31]. An essential feature of the $\text{Nd}_{2-x}\text{Sr}_x\text{NiO}_{4\pm\delta}$ reduction products was good reproducibility (Figure S10) and the enhanced stability of their catalytic properties in the DRM environment. This was illustrated by the results of the 45h stability test, which revealed only the minimum variation in the catalytic properties (Figure 6B). This stability could be affiliated with an absence of significant coking at the surface for the catalyst as one of the main reasons of catalyst deactivation during the DRM process (Figure S11).

3. Materials and Methods

$\text{Nd}_{2-x}\text{Sr}_x\text{NiO}_4$ ($x = 0 \div 1.4$) samples were obtained by the modified freeze-drying synthesis technique. To obtain multicomponent starting solutions, preliminarily calcined Nd_2O_3 and SrCO_3 were dissolved in the warm diluted acetic acid, then a $\text{Ni}(\text{NO}_3)_2 \cdot 6\text{H}_2\text{O}$ aqueous solution was added. To stabilize the frozen solution during freeze drying, an aqueous solution (5 wt. %) of polyvinyl alcohol was added to all solutions under intense stirring. The freeze-drying of flash-frozen solutions was performed at $P = 0.7$ mbar for 2 days. The thermal decomposition of the freeze-dried precursors was performed in the air at $800\text{--}1200$ °C for 6 h. A reduction in as-obtained $\text{Nd}_{2-x}\text{Sr}_x\text{NiO}_4$ powders was performed in an $\text{H}_2:\text{Ar} = 1:10$ gas mixture at different temperatures for 1 h, followed by slow cooling to room temperature under a reducing atmosphere.

XRD analysis of the powders was performed using a Rigaku D/MAX-2500PC diffractometer (Rigaku, Tokyo, Japan) with $\text{Cu K}\alpha$ radiation generated on a rotating Cu anode (40 kV, 250 mA). The profile analysis of the powder XRD data was carried out by the Le Bail method using the Jana 2006 program package. The TG-DSC thermal analysis of samples combined with a simultaneous QMS evolved gas analysis was performed in the air or in a 10% H_2/Ar gas mixture by STA 409PC/PG (NETZSCH) at $T = 40$ °C \div 1000 °C and a 10 K/min heating rate. The morphology of the powders was studied using a Carl Zeiss NVision 40 scanning electron microscope (Carl Zeiss SMT AG, Oberkochen, Germany).

The catalytic tests of the DRM reaction were carried out in a quartz glass flow fixed-bed reactor (18 mm internal diameter, 300 mm length) with a 0.2 g sample of the catalyst (100–250 mesh fraction) at atmospheric pressure in the absence of dilution with inert gas. This catalyst was first heated in a hydrogen flow at 10 K/min to 900 °C. Then, the gas stream was switched to a mixture of $\text{CH}_4/\text{CO}_2 = 1/1$ at GHSV values of 16 L/g h. No dilution in the feed flow by the inert gas was applied. The catalytic experiments were performed consecutively at 900, 800, 700, and 600 °C by holding at the preselected temperatures for 1–5 h at a steady state. After the analysis, the furnace was switched off, and the catalyst was cooled to room temperature over 3–4 h in pure N_2 . The details of the testing technique and GC analysis can be found elsewhere [34].

The methane conversion (X), product selectivity (S), and yield (Y) of the products were defined as follows:

$$X(\text{CH}_4, \%) = \frac{\text{moles of CH}_4 \text{ converted}}{\text{moles of CH}_4 \text{ in feed}} \times 100 \quad (8)$$

$$S(\text{CO}, \%) = \frac{\text{moles of CO in products}}{\text{moles of CH}_4 + \text{CO}_2 \text{ converted}} \times 100 \quad (9)$$

$$S(\text{H}_2, \%) = \frac{\text{moles of H}_2 \text{ produced}}{2 \times \text{moles of CH}_4 \text{ converted}} \times 100 \quad (10)$$

$$Y(\text{products}, \%) = \frac{X(\text{CH}_4, \%) \times S(\text{products}, \%)}{100} \quad (11)$$

$$\text{C balance } (\%) = \frac{\text{moles of C in products}}{\text{moles of C in feed}} \times 100 \quad (12)$$

The number of moles in the feed gases and gaseous products of the reactions was calculated based on the measured volumetric velocity of the feed gases and the products formed, as well as chromatography data, which made it possible to fully take into account the stoichiometry of the reaction and the corresponding volume expansion of the reacted gas mixture.

4. Conclusions

A full scale of the solid solutions $\text{Nd}_{2-x}\text{Sr}_x\text{NiO}_{4\pm\delta}$ ($0 \leq x \leq 1.4$) was obtained during these studies; the boundaries of their homogeneity ranged by the Nd/Sr ratio were refined.

The processes of a high-temperature reduction in these complex oxides were investigated; the composition and the morphology of as-obtained metal-oxide nanocomposites were determined. It was found that several Ni/(Nd₂O₃,SrCO₃) nanocomposites demonstrated outstanding activity and selectivity in the DRM process at T = 800 °C and the significant stability of their catalytic properties on stream. A positive effect of SrCO₃ on the catalytic properties of Ni/(Nd₂O₃,SrCO₃) nanocomposites was detected.

Supplementary Materials: The following supporting information can be downloaded at: <https://www.mdpi.com/article/10.3390/catal13060966/s1>. Figure S1: TG (green) and DSC (blue) profiles of freeze-dried Nd₂NiO₄ precursor, Figure S2: TG (green) and DSC (blue) profiles of freeze-dried Nd_{0.6}Sr_{1.4}NiO₄ precursor, Figure S3: XRD patterns of thermal decomposition products of Nd₂NiO₄ (x = 0) precursors at different temperatures, Figure S4: XRD patterns of thermal decomposition products of Nd_{1.5}Sr_{0.5}NiO₄ (x = 0.5) precursors at different temperatures, Figure S5: XRD patterns of thermal decomposition products of NdSrNiO₄ (x = 1) precursors at different temperatures, Figure S6: XRD patterns of thermal decomposition products of Nd_{0.8}Sr_{1.2}NiO₄ (x = 1.2) precursors at different temperatures, Figure S7: XRD patterns of thermal decomposition products of Nd_{0.6}Sr_{1.4}NiO₄ (x = 1.4) precursors at different temperatures, Figure S8: The dependence of Nd_{2-x}Sr_xNiO_{4±δ} lattice parameters on Sr content, Figure S9: CO₂ conversion (A) and H₂ yield (B) over the reduction products of various composites. The calculated values of H₂ yield are given according to [13,31–33], Figure S10: The results of testing the composites with various Sr content in the DRM process, Figure S11: SEM micrographs of the spent catalyst (x = 1.4).

Author Contributions: Conceptualization, O.A.S. and A.G.D.; methodology, O.A.S., S.A.M., A.S.L. and G.N.M.; validation, O.A.S., A.S.L. and G.N.M.; investigation, S.A.M., G.M.T., V.A., T.S. and I.V.R.; data curation, S.A.M. and A.S.L.; formal analysis, S.A.M., A.S.L.; software, S.A.M. and G.M.T.; resources, O.A.S. and A.S.L.; writing—original draft, O.A.S. and G.M.T.; Writing—review and editing, O.A.S., S.A.M., G.N.M. and A.S.L.; visualization, S.A.M. and G.M.T.; project administration, O.A.S. and A.G.D.; funding acquisition, O.A.S.; supervision, A.G.D. All authors have read and agreed to the published version of the manuscript.

Funding: This study is supported by the Russian Science Foundation (grant 22-23-00460). DRM experiments were carried out within the state funding of TIPS RAS. The Moscow State University program of development is gratefully acknowledged for the partial support of instrumental studies. SEM images were obtained at the IGIC RAS Joint Research Center for Physical Methods of Research.

Data Availability Statement: The data presented in this study are available in the present paper and supplementary materials.

Conflicts of Interest: The authors declare no conflict of interest.

References

1. Bhattar, S.; Abedin, M.A.; Kanitkar, S.; Spivey, J.J. A review on dry reforming of methane over perovskite derived catalysts. *Catal. Today* **2021**, *365*, 2–23. [[CrossRef](#)]
2. Moiseev, I.I.; Loktev, A.S.; Shlyakhtin, O.A.; Mazo, G.N.; Dedov, A.G. New approaches to the design of nickel, cobalt, and nickel-cobalt catalysts for partial oxidation and dry reforming of methane to synthesis gas. *Petrol. Chem.* **2019**, *59* (Suppl. S1), S1–S27. [[CrossRef](#)]
3. Wang, L.; Wang, F. Design Strategy, Synthesis, and Mechanism of Ni Catalysts for Methane Dry Reforming Reaction: Recent Advances and Future Perspectives. *Energy Fuels* **2022**, *36*, 5594–5621. [[CrossRef](#)]
4. Ranjekar, A.M.; Yadav, G.D. Dry reforming of methane for syngas production: A review and assessment of catalyst development and efficacy. *J. Indian Chem. Soc.* **2021**, *98*, 100002. [[CrossRef](#)]
5. Zhenghong, B.; Fei, Y. Catalytic conversion of biogas to syngas via dry reforming process. *Adv. Bioenergy* **2018**, *3*, 43–76.
6. Gao, Y.; Jiang, J.; Meng, Y.; Yan, F.; Aihemaiti, A. A review of recent developments in hydrogen production via biogas dry reforming. *Energy Convers. Manag.* **2018**, *171*, 133–155. [[CrossRef](#)]
7. Rosha, P.; Rosha, A.K.; Ibrahim, H.; Kumar, S. Recent advances in biogas upgrading to value added products: A review. *Int. J. Hydrogen Energy* **2021**, *46*, 21318–21337. [[CrossRef](#)]
8. Abdulrasheed, A.; Abdul Jalil, A.; Gambo, Y.; Ibrahim, M.; Hambali, H.U.; Shahul Hamid, M.Y. A review on catalyst development for dry reforming of methane to syngas: Recent advances. *Renew. Sustain. Energy Rev.* **2019**, *108*, 175–193. [[CrossRef](#)]
9. Aramouni, N.A.K.; Touma, J.G.; Tarboush, B.A.; Zeaiter, J.; Ahmad, M.N. Catalyst design for dry reforming of methane: Analysis review. *Renew. Sustain. Energy Rev.* **2018**, *82*, 2570–2585. [[CrossRef](#)]
10. Li, M.; Sun, Z.; Hu, Y.H. Catalysts for CO₂ reforming of CH₄: A review. *J. Mater. Chem. A* **2021**, *9*, 12495. [[CrossRef](#)]

11. Arora, S.; Prasad, R. An overview on dry reforming of methane: Strategies to reduce carbonaceous deactivation of catalysts. *RSC Adv.* **2016**, *6*, 108668. [[CrossRef](#)]
12. Papadopoulou, C.; Matralis, H.; Verykios, X. Utilization of Biogas as a Renewable Carbon Source: Dry Reforming of Methane. In *Catalysis for Alternative Energy Generation*; Gucci, L., Erdöhelyi, A., Eds.; Springer: New York, NY, USA, 2012; pp. 57–127.
13. Le Sache, E.; Reina, T.R. Analysis of Dry Reforming as direct route for gas phase CO₂ conversion. The past, the present and future of catalytic DRM technologies. *Prog. Energy Combust. Sci.* **2022**, *89*, 100970. [[CrossRef](#)]
14. Liu, Z.; Lustemberg, P.; Gutierrez, R.A.; Carey, J.J.; Palomino, R.M.; Vorokhta, M.; Grinter, D.C.; Ramirez, P.J.; Matolin, V.; Nolan, M.; et al. In Situ Investigation of Methane Dry Reforming on Metal/Ceria(111) Surfaces: Metal–Support Interactions and C-H Bond Activation at Low Temperature. *Angew. Chem. Int. Ed.* **2017**, *56*, 13041–13046. [[CrossRef](#)] [[PubMed](#)]
15. Liu, Z.; Grinter, D.C.; Lustemberg, P.G.; Nguyen-Phan, T.-D.; Zhou, Y.; Luo, S.; Waluyo, I.; Crumlin, E.J.; Stacchiola, D.J.; Zhou, J.; et al. Dry Reforming of Methane on a Highly-Active Ni-CeO₂ Catalyst: Effects of Metal-Support Interactions on C-H Bond Breaking. *Angew. Chem. Int. Ed.* **2016**, *55*, 7455–7459. [[CrossRef](#)] [[PubMed](#)]
16. Batiot-Dupeyrat, C.; Gallego, G.A.S.; Mondragon, F.; Barrault, J.; Tatibouët, J.-M. CO₂ reforming of methane over LaNiO₃ as precursor material. *Catal. Today* **2005**, *107–108*, 474–480. [[CrossRef](#)]
17. Bonmassar, N.; Bekheet, M.F.; Schlicker, L.; Gili, A.; Gurlo, A.; Doran, A.; Gao, Y.; Heggen, M.; Bernardi, J.; Klötzer, B.; et al. In Situ-Determined Catalytically Active State of LaNiO₃ in Methane Dry Reforming. *ACS Catal.* **2020**, *10*, 1102–1112. [[CrossRef](#)]
18. Tarutin, A.P.; Lyagaeva, J.G.; Medvedev, D.A.; Bi, L.; Yaremchenko, A. Recent advances in layered Ln₂NiO_{4+δ} nickelates: Fundamentals and prospects of their applications in protonic ceramic fuel and electrolysis cells. *J. Mater. Chem. A* **2021**, *9*, 154–195. [[CrossRef](#)]
19. Shlyakhtin, O.A.; Malyshev, S.A.; Loktev, A.S.; Mazo, G.N.; Garshev, A.V.; Chumakov, R.G.; Dedov, A.G. Synthesis and decomposition of Nd_{2–y}Ca_yCo_{1–x}Ni_xO₄: The effect of resynthesis on the catalytic performance of decomposition products in the partial oxidation of methane. *ACS Appl. Energy Mater.* **2021**, *4*, 7661–7673. [[CrossRef](#)]
20. Malyshev, S.A.; Shlyakhtin, O.A.; Loktev, A.S.; Mazo, G.N.; Timofeev, G.M.; Mukhin, I.E.; Kaplin, I.Y.; Svetogorov, R.D.; Valeev, R.G.; Dedov, A.G. Exsolution-like synthesis of Ni/(Nd₂O₃,CaO) nanocomposites from Nd_{2–x}Ca_xNiO₄ precursors for catalytic applications. *J. Solid State Chem.* **2022**, *312*, 123267. [[CrossRef](#)]
21. Malyshev, S.A.; Shlyakhtin, O.A.; Loktev, A.S.; Mazo, G.N.; Timofeev, G.M.; Mukhin, I.E.; Svetogorov, R.D.; Roslyakov, I.V.; Dedov, A.G. Ni/(R₂O₃,CaO) nanocomposites produced by the exsolution of R_{1.5}Ca_{0.5}NiO₄ nickelates (R = Nd, Sm, Eu): Rare earth effect on the catalytic performance in the dry reforming and partial oxidation of methane. *Materials* **2022**, *15*, 7265. [[CrossRef](#)]
22. Kwon, O.; Joo, S.; Choi, S.; Sengodan, S.; Kim, G. Review on exsolution and its driving forces in perovskites. *J. Phys. Energy* **2020**, *2*, 032001. [[CrossRef](#)]
23. Tsekouras, G.; Miller, D.N.; Ménard, H.; Irvine, J.T.S. In situ growth of nanoparticles through control of non-stoichiometry. *Nat. Chem.* **2013**, *5*, 916–923.
24. Shah, S.; Sayono, S.; Junzunza, J.; Pan, R.; Xu, M.; Pan, X.; Gilliard-AbdulAziz, K.L. The effects of stoichiometry on the properties of exsolved Ni-Fe alloy nanoparticles for dry methane reforming. *AIChE J.* **2020**, *66*, e17078. [[CrossRef](#)]
25. Neagu, D.; Oh, T.S.; Miller, D.N.; Ménard, H.; Bukhari, S.M.; Gamble, S.R.; Gorte, R.J.; Vohs, J.M.; Irvine, J.T.S. Nano-socketed nickel particles with enhanced coking resistance grown in situ by redox exsolution. *Nat. Commun.* **2015**, *6*, 8120. [[CrossRef](#)] [[PubMed](#)]
26. Steiger, P.; Nachtegaal, M.; Kröcher, O.; Ferri, D. Reversible segregation of Ni in LaFe_{0.8}Ni_{0.2}O_{3±δ} during coke removal. *ChemCatChem* **2018**, *10*, 4456–4464. [[CrossRef](#)]
27. Takeda, Y.; Nishijima, M.; Imanishi, N.; Kanno, R.; Yamamoto, O.; Takano, M. Crystal chemistry and transport properties of Nd_{2–x}A_xNiO₄ (A = Ca, Sr, or Ba, 0 ≤ x ≤ 1.4). *J. Solid State Chem.* **1992**, *96*, 72–83. [[CrossRef](#)]
28. Blasco, J.; Garsia, J. A comparative study of the crystallographic, magnetic and electrical properties of the Nd_{1–x}La_xNiO_{3–δ} system. *J. Phys. Condens. Matter* **1994**, *6*, 10759–10772. [[CrossRef](#)]
29. Malyshev, S.A.; Shlyakhtin, O.A.; Mazo, G.N.; Garshev, A.V.; Mironov, A.V.; Loktev, A.S.; Dedov, A.G. Comparative analysis of NdCaCoO₄ phase formation from cryogel and from solid state precursors. *J. Sol-Gel Sci. Technol.* **2017**, *81*, 372–377. [[CrossRef](#)]
30. Omata, K.; Nukui, N.; Hottai, T.; Showa, Y.; Yamada, M. Strontium carbonate supported cobalt catalyst for dry reforming of methane under pressure. *Catal. Commun.* **2004**, *5*, 755–758. [[CrossRef](#)]
31. Han, K.; Wang, S.; Hu, N.; Shi, W.; Wang, F. Alloying Ni–Cu Nanoparticles Encapsulated in SiO₂ Nanospheres for Synergistic Catalysts in CO₂ Reforming with Methane Reaction. *ACS Appl. Mater. Interfaces* **2022**, *14*, 23487–23495. [[CrossRef](#)]
32. Shi, Y.; Han, K.; Wang, F. Ni–Cu Alloy Nanoparticles Confined by Physical Encapsulation with SiO₂ and Chemical Metal–Support Interaction with CeO₂ for Methane Dry Reforming. *Inorg. Chem.* **2022**, *61*, 15619–15628. [[CrossRef](#)] [[PubMed](#)]
33. Cai, X.; Hu, Y.H. Advances in catalytic conversion of methane and carbon dioxide to highly valuable products. *Energy Sci. Eng.* **2019**, *7*, 4–29. [[CrossRef](#)]
34. Gavrikov, A.V.; Loktev, A.S.; Ilyukhin, A.B.; Mukhin, I.E.; Bykov, M.A.; Maslakov, K.I.; Vorobei, A.M.; Parenago, O.O.; Sadovnikov, A.A.; Dedov, A.G. Supercritical fluid-assisted modification combined with the resynthesis of SmCoO₃ as an effective tool to enhance the long-term performance of SmCoO₃-derived catalysts for the dry reforming of methane to syngas. *Dalton Trans.* **2022**, *51*, 18446–18461. [[CrossRef](#)] [[PubMed](#)]

Disclaimer/Publisher’s Note: The statements, opinions and data contained in all publications are solely those of the individual author(s) and contributor(s) and not of MDPI and/or the editor(s). MDPI and/or the editor(s) disclaim responsibility for any injury to people or property resulting from any ideas, methods, instructions or products referred to in the content.